Micro and Nanostructures 210 (2026) 208513

Contents lists available at ScienceDirect

Micro and Nanostructures

journal homepage: www.journals.elsevier.com/micro-and-nanostructures

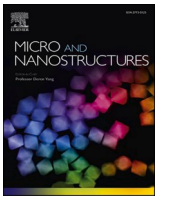

Investigation of latent fingerprints on porous and non-porous surfaces using multi-walled carbon nanotube-assisted ZnO nanocomposites

Basavajyothi Khapate [a], Bhavani Betadur [b], Madhura N. Talwar [c], Asha P. Shirni [c], Milana Nagaraj [a], Kotresh M. Goudar [b], Gnanaprakash A.P. [c], Pushpa N. [a,*]

[a] PG Department of Physics, JSS College of Arts, Commerce and Science, Ooty Road, Mysuru, 570025, India
[b] Department of Studies in Physics, Vijayanagara Sri Krishnadevaraya University, Ballari, 583105, India
[c] Department of Studies in Physics, University of Mysore, Manasagangotri, Mysuru, 570006, India

ARTICLE INFO

Keywords:
ZnO:MWCNT nanocomposites
Rietveld refinement
Burstein–moss effect
Resolution ratio, anti-counterfeiting

ABSTRACT

An innovative, safe, cost-effective, and eco-friendly multi-walled carbon nanotubes (MWCNTs)-assisted Zinc oxide (ZnO) nanocomposites (NCs) were synthesized using a low-temperature solution combustion method followed by ex-situ ultrasonication. The X-ray diffraction (XRD) and field-emission scanning electron microscope (FESEM) results revealed that MWCNT doping did not affect the phase structure; however, a decrease in average crystallite size was observed, from 48.14 nm to 37.07 nm. Ultraviolet–visible (UV) spectroscopy studies revealed an increase in optical bandgap with MWCNTs doping. The photoluminescence (PL) spectra at different excitation wavelengths showed maximum emission at 364, 369 and 362 nm, attributed to the near-band-edge emission of ZnO. The ZnO:MWCNT NCs were successfully used to investigate latent fingerprints (LFPs) on both porous and non-porous surfaces. These NCs showed excellent stability under humidity, temperature and mechanical abrasion tests. Further analysis highlights the average ridge spacing of 0.236 mm with a resolution ratio of 4.24 ridges/mm on porous surfaces, and on non-porous surfaces, it was noted as 0.251 mm, yielding a resolution ratio of 3.98 ridges/mm, confirming significant image resolution. These outcomes indicate that these high-performance ZnO:MWCNT NCs have potential applications in LFPs detection.

1. Introduction

Forensic science involves the application of scientific methods to investigate criminal activities and analyse evidence for legal proceedings [1]. Among its many disciplines, fingerprint (FP) analysis, known as dactyloscopy, remains one of the most reliable methods for personal identification [2]. FPs are unintentionally left at crime scenes by offenders and are generally classified as plastic, patent and latent fingerprints (LFP) [3].

LFPs are formed by sweat secretions from the eccrine, apocrine and sebaceous glands [4] and are unique and remain unchanged throughout an individual's lifetime. These FPs are analysed at three hierarchical levels. Level I features include general ridge flow patterns such as arches, whorls and loops. Level II features comprise ridge endings, bifurcations, islands and lakes [5,6]. Level III

* Corresponding author.
E-mail address: pushpagnp1975@gmail.com (N. Pushpa).

https://doi.org/10.1016/j.micrna.2025.208513
Received 26 July 2025; Received in revised form 24 November 2025; Accepted 2 December 2025
Available online 3 December 2025

Table 1
A comparative study of the present work and the previously reported NCs for LFP detection.

Material	Method	Crystallite size (nm)	PL Excitation wavelength (nm)	PL emission wavelength (nm)	CIE	CCT (K)	Substrates	LFP detection	Reference
La_2CaZnO_5: 1mol% Er^{3+}	Solution combustion	50.60	378	549	(0.3158, 0.6636)	5753	Paper, OHP, Al foil, plastic, steel, glass	Level I, II and III	[11]
$CaY_2Sb_2(ZnO_4)_3$:10 mol% Sm^{3+}	High-temperature solid-state method	10.4	407	610	(0.585, 0.414)	5674	Steel, plastic, glass	Up to level III	[12]
$BaTiO_3$:2 mol % Dy^{3+}	Ultrasound-assisted sonochemical	36	387	574	(0.3346, 0.3407)	5403	Green leaf, plastic sheet, pen edge, TV remote, mobile screen	Only fingerprint images	[13]
$Ca_{99.5}WO_4$:0.5 mol% Sm^{3+}	Solid-state reaction	42.13	250	640	(0.635, 0.364)	2114	Al foil, stapler, spoon	Only the fingerprint image	[14]
TiO_2: 1 mol% Ce^{3+}	Solution combustion	26	396	544	(0.3582, 0.3951)	4563	Al foil	Level I, II and III	[15]
PVA/Gd_2O_3: 5 mol %Eu^{3+}	Solution casting route	32	394	710	–	4396	Glass, Al foil, stainless steel	Level I and II	[16]
$NaYF_4$:20 %Yb, 2 %Er, 15 %Fe UCNPs	Hydrothermal method	27.32	980 nm (laser irradiation)	655	–	–	Glass, table, paper, iron sheet, credit card	Level I, II and III	[17]
$SrZrO_3$: 5 mol% Sm^{3+}	Solution combustion technique	48	403	609	(0.6362, 0.3633)	2724	Mobile screen	Level I, II and III	[18]
$Zn_{0.95}Cu_{0.05}O$ nanoparticles	Co-precipitation method	18.48	325	478	–	–	Wood sheet, metal scale, book wrapper, plastic sheet, coin	Level I, II and III	[19]
ZnO	Chemical precipitation	23.7	325	606	–	–	Al foil, black glass, clear glass, steel	Level I and II	[20]
$NaYF_4$:20 %Yb, 2 %Er, 30 % Mn	Hydrothermal method	180	980 (NIR)	653	(0.523, 0.451)	–	Glass, plastic, ceramic tile, tron sheet, paper, banknotes	Level I, II and III	[21]
Y_2SrZnO_5: 20 mol% Eu^{3+}	Self-igniting combustion	50	393 (near UV) 465	595 612	(0.630,0.369)	1160	Porous, semi-porous and non-porous	Level I, II and III	[22]
Y_2O_3: 7 mol%Fe^{3+}	Solution combustion method	18	266	383	(0.1830, 0.4491)	10628	Leaf, Al foil, marble	Level I, II and III	[23]
Ca_2InTaO_6:0.40Eu^{3+}	High-temperature solid-state reaction	54.8	395	613	(0.327, 0.339)	5748	Al foil, glass, paper, plastic	Level I, II and III	[24]
ZnO:4 wt% MWCNT	Solution combustion + Ultrasonication	37.68	260	363	(0.156, 0.023)	1756	Glass sheet, acrylic sheet, wood, granite, Al foil	Level I, II and III	**Present work**

features, including pore structure, ridge shapes, creases, scars and warts, provide the most detailed information for individual identification [7]. Since LFPs are invisible to the naked eye, their visualisation requires enhancement techniques.

There are many studies, like traditional black powders, ninhydrin or DFO (1,8-diazafluoren -9-one), used by forensic investigators in revealing LFPs. But as they are larger in size compared to nanocomposites, they exhibit limited capability in revealing ridge details, are effective only on porous surfaces such as paper and cardboard and require necessary temperature and humidity controls for visualising LFPs [8]. Moreover, DFO compounds contain toxic and carcinogenic substances that are harmful to forensic examiners [9, 10]. These limitations prompted the researchers to explore various alternatives for visualising LFPs. One such approach involves the application of luminescent powders. When these powders are dusted onto the LFPs, they adhere to them and glow under ultraviolet light of different wavelengths, allowing for the examination of intricate details of the LFPs.

Many rare-earth doped metal oxide NCs used as luminescent powders have demonstrated superior optical properties compared to bulk metal oxides in visualising LFPs. Table 1 shows a comparison of several hosts doped with rare earth elements and metal oxides, along with the level of visualising FPs on various surfaces. Among the metal oxides, ZnO is the most extensively studied owing to its non-toxic nature, wide bandgap, high exciton binding energy (~60 meV) and ability to function as a transparent conductive oxide [20, 25]. These properties make ZnO highly suitable for applications in photocatalysis, gas sensing, solar cells, LEDs, and forensic sciences [20,27]. While rare-earth-doped metal oxide NCs have demonstrated superior optical properties compared to bulk, the high cost and short supply of rare-earth elements have driven an urgent need for sustainable alternatives [26,28]. Carbon nanotubes (CNTs), particularly MWCNTs, have emerged as promising nanomaterials due to their exceptional electrical, optical and biological properties [29]. These are widely used in photocatalysis, gas sensing, energy storage, anti-fouling coatings, construction materials and display technologies [30–35].

Recent studies support the use of MWCNT as dopants. Ahmadipour et al. report that the mixing of 0.2 wt% MWCNT to calcium copper titanate exhibits the highest dielectric permittivity and the lowest dielectric loss for electronic device applications [36]. Jazi et al. prepared ZnO/MWCNT NCs for biomolecule detection, exhibiting high performance in glucose detection [37]. Ardani et al. investigated polyaniline-MWCNT NCs via the ultrasonic method, showing excellent photocatalytic performance with 7 wt% MWCNT [38]. Zargar et al. synthesized MWCNT-ZnO thick films via a sol-gel screen printing method for LED applications [39].

Despite these advancements, research on ZnO:MWCNT NCs for anti-counterfeiting and forensic applications has remained unexplored. Therefore, this work aims to study the effect of varying MWCNT concentrations on the optical properties of ZnO nanoparticles. ZnO:MWCNT NCs with various amounts of MWCNT were synthesized and systematically used for the visualisation of LFPs on various porous and non-porous surfaces. The results of the study are expected to present an innovative, cost-effective, sustainable alternative for high-resolution visualisation of LFP to existing commercial powders and rare-earth-doped NCs.

2. Experimental section

2.1. Materials

The chemicals Zinc nitrate hexahydrate ($Zn(NO_3)_2.6H_2O$, 98 % pure) and oxalic acid ($C_2H_2O_4.2H_2O$, 99 % pure) were purchased from LOBA Chemie Pvt. Ltd and Molychem company, respectively. MWCNTs (99 % pure) were procured from Vedayukt India Private Limited. Double-distilled water and ethanol were used as the solvents in the chemical reactions. All the chemicals were of utmost purity, hence used without any further refining.

Fig. 1. Flowchart illustrating the combustion synthesis of ZnO and ZnO:MWCNT **NCs**.

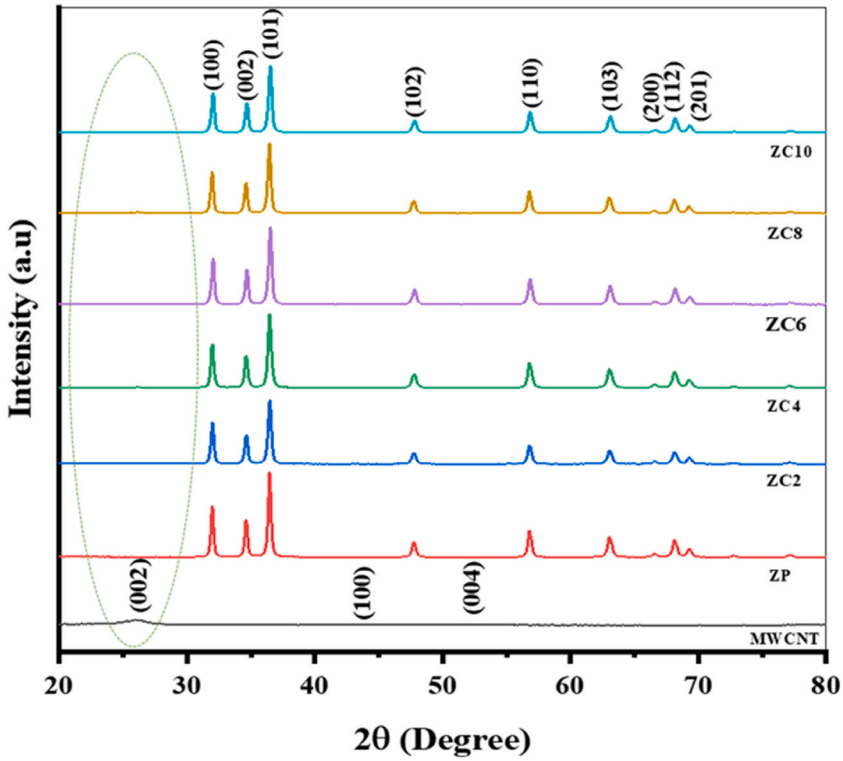

Fig. 2. XRD patterns of ZnO, MWCNT and ZnO:MWCNT **NCs**.

2.2. Synthesis of ZnO: xMWCNTs (x = 0, 2, 4, 6, 8 and 10 wt%) nanocomposites

A low-temperature solution combustion method was used to synthesize the ZnO nanoparticles. Zinc nitrate hexahydrate and oxalic acid were used as the oxidiser and fuel, respectively. MWCNTs were used as the dopant.

Initially, the oxidiser and the fuel, both possessing low decomposition temperatures, were dissolved separately in distilled water using a magnetic stirrer for 30 min. Subsequently, the solutions were combined into a single beaker, allowing the fuel to complex with metal ions, thus promoting a uniform mixture and were stirred for an additional 30 min. The resulting solution was then placed in a preheated muffle furnace at 300 °C. An exothermic reaction occurred during which nitrates were oxidised, releasing nitrogen (N_2), oxygen (O_2) and water vapours, while the fuel acted as a reducing agent, releasing carbon. The resulting voluminous, foamy and fluffy material was transferred to a crucible and calcined at 500 °C for 2 h in a muffle furnace to enhance crystallinity and eliminate residual organic impurities.

The synthesized ZnO nanoparticles were then used to prepare ZnO:xMWCNT (x = 0, 2, 4, 6, 8 and 10 wt%; denoted as ZP, ZC2, ZC4, ZC6, ZC8 and ZC10, respectively) NCs. Due to the hydrophobic nature of MWCNTs, they do not disperse easily in water. Therefore, ethanol was used as the solvent in an ex-situ synthesis approach to prepare the various compositions. The ex-situ ultrasonication method is chosen for synthesizing ZnO: MWCNT NCs due to its simplicity, efficiency and ability to provide excellent dispersion of ZnO nanoparticles onto MWCNTs without subjecting the delicate nanostructures to harsh conditions that may occur in in-situ synthesis methods. Ultrasonication produces intense local forces in the liquid, effectively breaking up any nanoparticle agglomerates and dispersing both components, ensuring uniform contact and better coverage of ZnO on the MWCNT surface. The ex-situ ultrasonication largely preserves the original crystal structure of ZnO and minimises the formation of defects at the ZnO: MWCNT interface. The high

Table 2
Crystallite size of pristine ZnO and ZnO:MWCNT NCs.

Sample	Average crystallite size D (nm)		Dislocation density (δ x10^{-3} nm^{-2})		Micro strain
	DS Method	W–H Method	DS Method	W–H Method	(ε x10^{-3})
ZP	**25.69**	**48.14**	**1.59**	**0.43**	**1.61**
ZC2	**23.77**	**36.97**	**1.83**	**0.73**	**1.32**
ZC4	**22.98**	**37.68**	**1.97**	**0.70**	**1.49**
ZC6	**24.17**	**38.52**	**1.77**	**0.67**	**1.35**
ZC8	**24.92**	**41.14**	**1.67**	**0.59**	**1.40**
ZC10	**23.68**	**37.07**	**1.84**	**0.72**	**1.34**

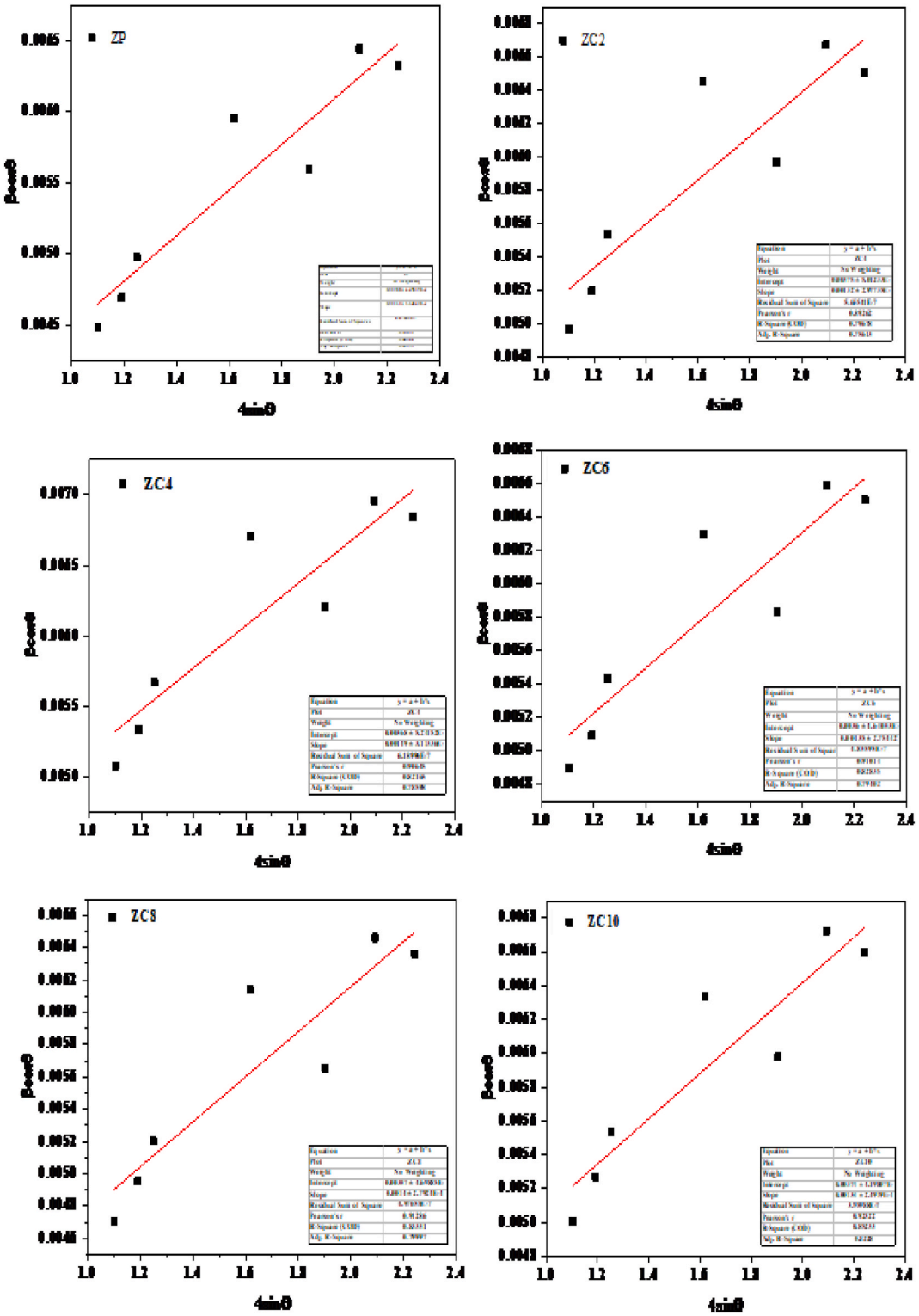

Fig. 3. Williamson-Hall plot of ZnO:MWCNT NCs.

crystal quality ensures good material stability, which is essential for investigating LFPs. Excess or uncontrolled defect formation, as in in-situ synthesis methods, can degrade the nanocomposite stability and performance of NCs. In this method, the samples were ultrasonicated at 50 °C for 1 h. The resulting dispersions were then dried in a hot-air oven at 60 °C for 1 h to remove moisture. A

detailed synthesis flowchart of the nanocomposites is illustrated in Fig. 1.

2.3. Material characterization

The XRD patterns were analysed using an Empyrean diffractometer with Cu-Kα radiation (λ = 0.154 Å), and diffraction patterns were measured within a 2θ range of 10° - 80° with a step size of 0.02. The morphological analysis was done using a FESEM HITACHI SU6600 microscope, and elemental compositions of the samples were examined employing an energy dispersive spectrometer. The vibrational chemical bonding between elements was assessed using a Fourier transform infrared spectroscopy (FTIR) PerkinElmer Spectrum Two FT-IR spectrometer, monitored at room temperature, covering a range of 400–4000 cm^{-1}. The Raman studies were conducted to confirm the dispersion of MWCNT in ZnO:MWCNT NCs using a Horiba Scientific spectrometer. The optical excitation wavelength for each sample was determined at room temperature, using a UV AU-2703 Systronics Limited spectrophotometer. A xenon lamp served as the excitation source with ethanol as the solvent for this measurement. The PL spectra were measured on a SHIMADZU RF-6000 spectrofluorophotometer.

2.4. Visualisation of LFP techniques

To visualise LFPs, volunteers were instructed to wash their hands thoroughly with soap and water. They were then asked to rub their fingers gently against their forehead or nose to transfer sebaceous secretions and subsequently press their fingers onto different surfaces (glass sheet, acrylic, aluminium foil, granite and wood) for 3–5 s. The LFP impressions were then developed using the powder dusting technique. The NCs ZC4 and ZC8 were used as fluorescent dusting powders, applied with a soft feather brush. The developed FP images were obtained under both normal daylight and UV light at 365 nm.

3. Results and discussion

3.1. Structural analysis

The crystallinity of MWCNT, ZnO nanoparticles and ZnO:xMWCNT NCs was studied using the XRD technique. The XRD spectra of the prepared samples measured at room temperature are as shown in Fig. 2. The peaks present at the planes (100), (002), (101), (102), (110), (103), (200), (112) and (201) of the prepared samples match well with the ICDD data card no. 00-36-1451 [20]. The diffraction

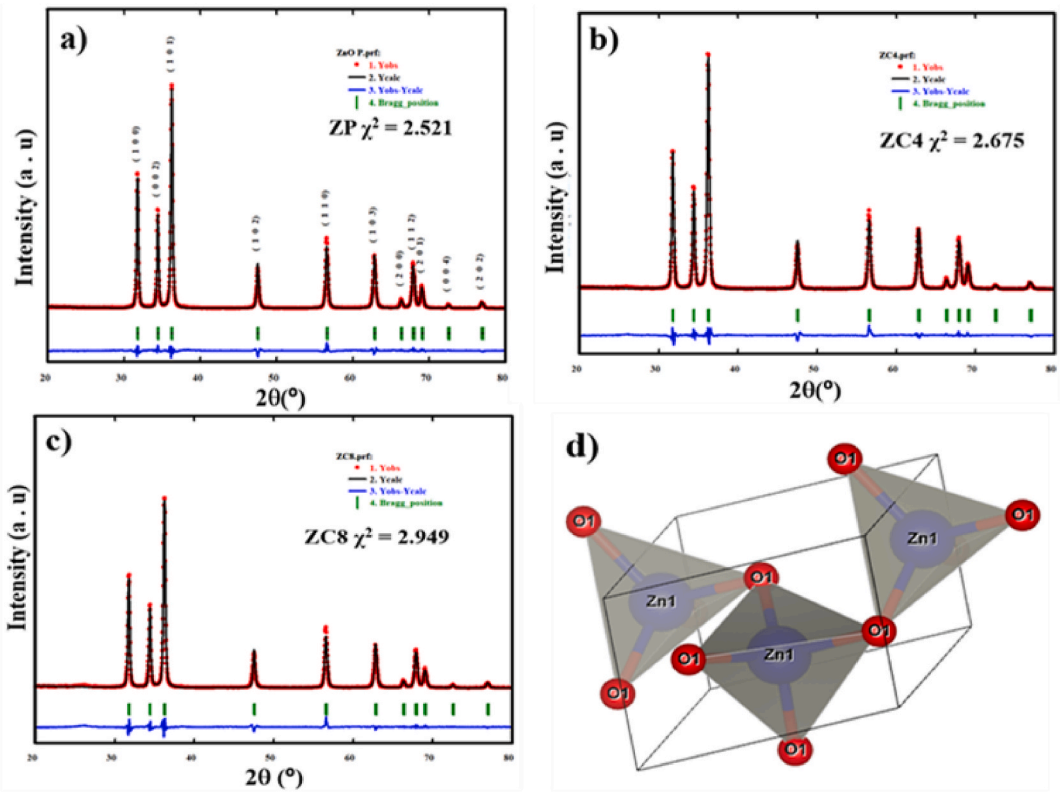

Fig. 4. Rietveld plot of a) ZnO, b) ZC4, c) ZC8 and d) crystal structure of ZnO.

Table 3
Rietveld refined parameters of ZnO and ZnO:MWCNT **NCs**.

Compound	ZnO	ZC4	ZC8
Number of space group	186	186	186
Hermann-Mauguin symbol	P 63 m c	P 63 m c	P 63 m c
Hall symbol	P 6 c -2c	P 6 c -2c	P 6 c -2c
Crystal system	Hexagonal	Hexagonal	Hexagonal
Bravais lattice	P	P	P
Density (g/cm^3)	5.681	5.714	5.654
a=b(Å)	3.2520	3.2521	3.2527
c(Å)	5.2102	5.2105	5.2112
$\alpha = \beta$ (^{0})	90	90	90
γ (^{0})	120	120	120
Volume ($Å^3$)	47.7171	47.7250	47.7481
R_p%	8.88	9.83	11.9
R_{wp}%	11.6	12.0	13.7
R_e%	7.29	7.32	8.01
χ^2	2.521	2.675	2.949

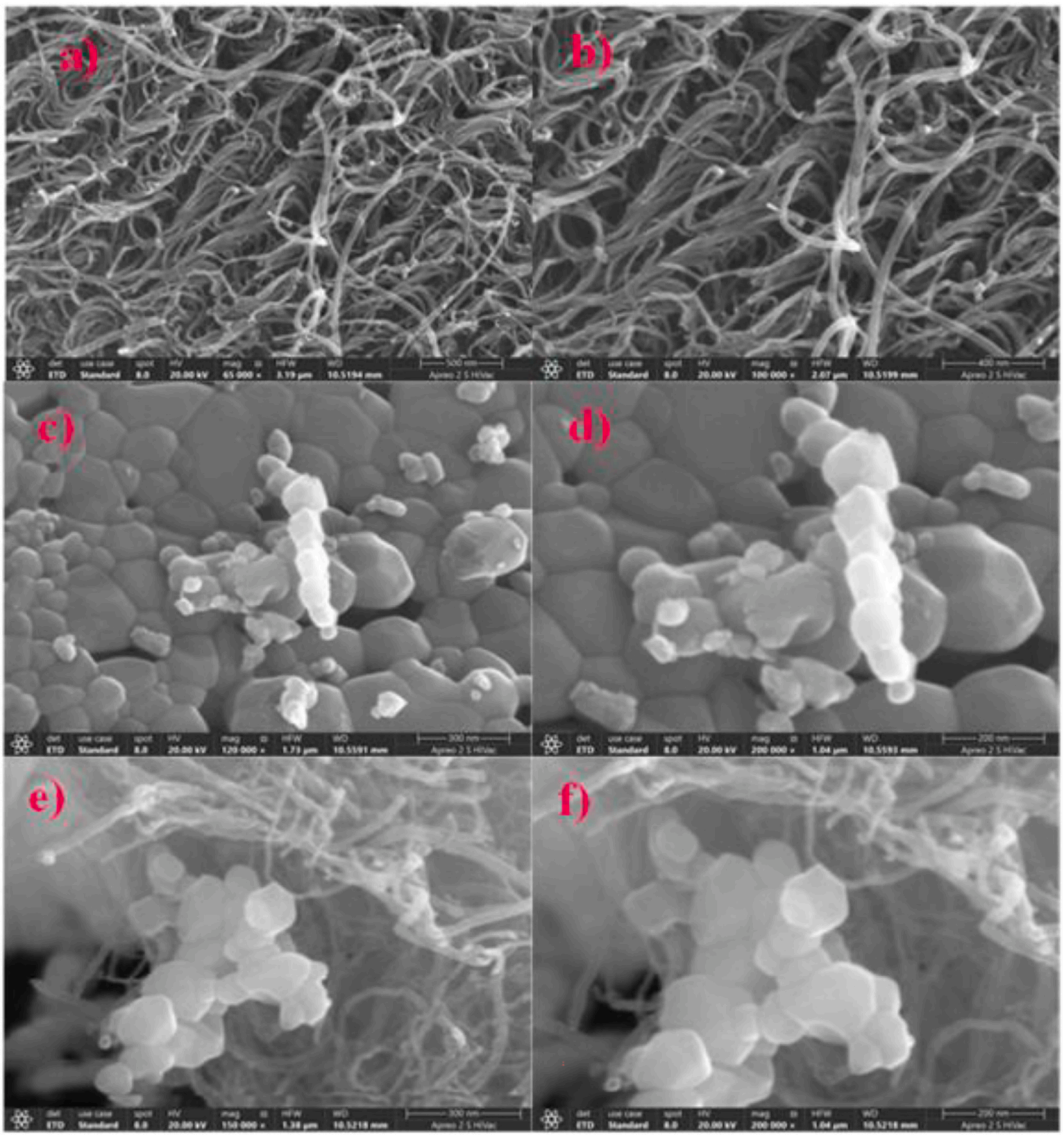

Fig. 5. FE-SEM micrographs of a, b) MWCNT, c, d) Pristine ZnO and e, f) ZnO: 8 wt% MWCNT NCs.

peaks of MWCNT at (002) and (100) planes are in good agreement with the JCPDS card no. 25–0284 [30]. The absence of additional peaks in the diffraction pattern confirms that the phase purity and crystalline structure of ZnO remain unaltered even after doping with MWCNT. However, a slight shift toward higher angles in the diffraction peaks was observed at doping concentrations of 6 wt% to 10 wt % of MWCNT. This could be attributed to the interaction between ZnO and MWCNT occurring at the surface rather than penetrating deep into the crystal structure of the ZnO nanoparticles.

The value of the average crystallite size (D) of the NCs was calculated using Debye-Scherrer's (DS) equation,

$$D = \frac{k\lambda}{\beta \cos\theta} \tag{1}$$

where 'k' represents an empirical constant, λ is the wavelength of the X-ray source, β is the full width at half maximum (FWHM) in radians for all (hkl) indexed peaks and θ (in ^{0}) is the Bragg's diffraction angle position of all the peaks. The calculated values of crystallite size for the prepared samples are listed in Table 2. The use of Debye-Scherrer's equation for crystallite size estimation ignores lattice strain and considers crystallite size effects only due to all XRD peak broadening [48]. This limitation in the present study was addressed by using Williamson-Hall (W–H) analysis to calculate crystallite size, dislocation density, and microstrain. The equation that can represent the effect of crystallite size and micro strain on FWHM is given by

$$\boldsymbol{\beta \cos\theta = \varepsilon(4 \sin\theta) + \frac{0.9\lambda}{D}} \tag{2}$$

Where $\boldsymbol{\beta}$ is the FWHM (in radians), $\boldsymbol{\theta}$ is the Bragg angle of the peak, $\boldsymbol{\varepsilon}$ is the strain ascribed to the NCs, $\boldsymbol{\lambda}$ is the X-ray diffraction wavelength, and D is the crystallite size. As the above equation represents a straight line, hence $\boldsymbol{4 \sin\theta}$ is plotted along the x-axis and $\boldsymbol{\beta \cos\theta}$ is plotted along the y-axis as shown in Fig. 3. The slope of the line gives the strain ($\boldsymbol{\varepsilon}$) and $\left(\frac{0.9\lambda}{D}\right)$ the intercept of this line gives the crystallite size D. The dislocation density is calculated using the following equation

$$\text{Dislocation density}, \boldsymbol{\delta} = \frac{\mathbf{1}}{\boldsymbol{D^2}} \tag{3}$$

The summary of the crystallite size, dislocation density and micro-strain calculated from the DS method and WH-analysis is shown in Table 2. The variation in the crystallite size with increasing dopant concentration was mainly considered as a result of peak broadening, as the DS method does not consider lattice strain. In contrast, the increased crystallite size values obtained from the WH analysis can be attributed to the inclusion of micro-strain effects. The variation in the dislocation density and micro strain presented in Table 2 is due to the defects generated in the crystal structure with increasing MWCNT concentration.

To investigate the structural attributes of the NCs in greater detail, the Rietveld refinement approach was used with FullProf software. A strong correlation between the generated XRD pattern with the experimental one is observed. The crystallite size of the ZC4 sample is smaller than that of pristine ZnO, while the crystallite size of ZC8 increased following MWCNT doping compared to the other samples. Hence, these samples were considered for further studies. The XRD data for these samples were refined using Rietveld refinement methods, which are shown in Fig. 4(a–c). The Pseudo-Voigt peak profile function was employed for optimal refinement. The observed and calculated patterns are shown in red and black colour line curves, respectively. The blue and green colour lines represent the difference between observed and calculated values and Bragg's position, respectively. The reliability factors for the ultimate calibration coefficients R_p, R_{wp}, Chi^2 and other parameters are detailed in Table 3. By employing the refined values, a packing diagram was generated with VESTA software and is displayed in Fig. 4d.

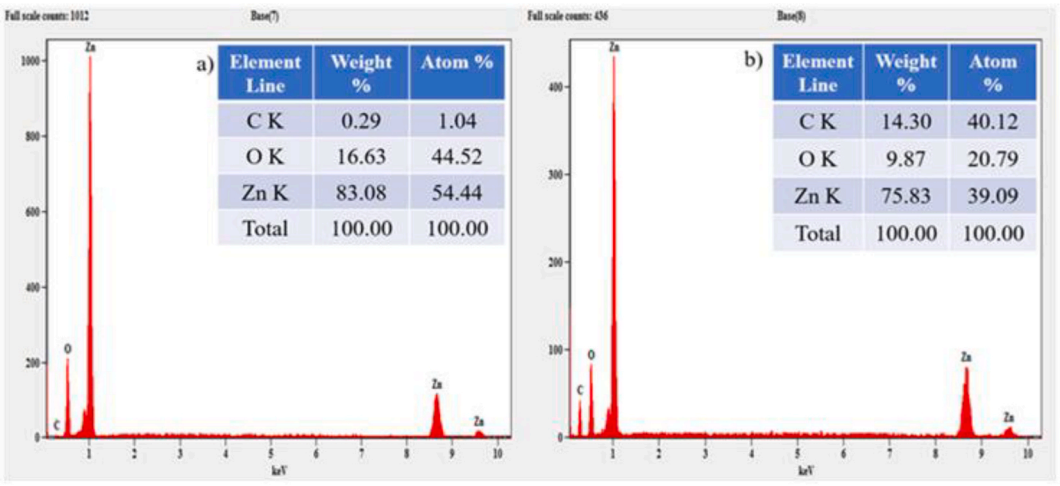

Fig. 6. EDAX micrographs of a) pristine ZnO and b) ZnO:MWCNT NCs.

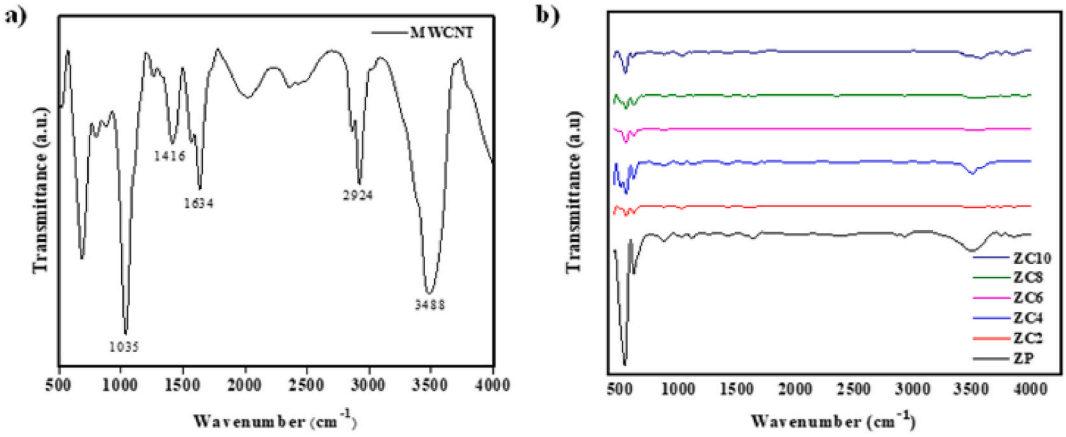

Fig. 7. FTIR spectra of a) MWCNT and b) ZnO:MWCNT **NCs**.

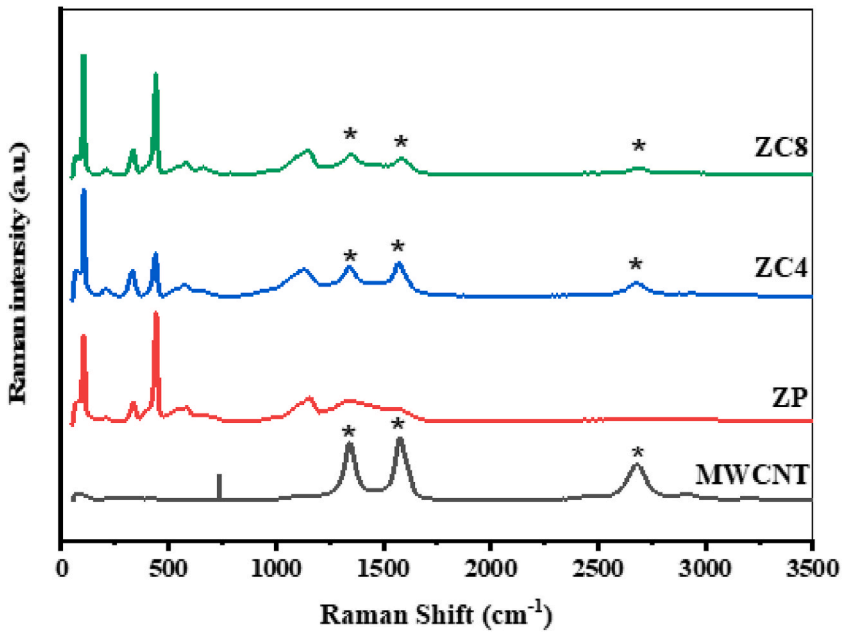

Fig. 8. Raman spectra of MWCNT, ZnO and ZnO:MWCNT NCs.

The increase in χ^2 values observed with higher doping concentrations can be analysed as a result of changes in the diffraction pattern, primarily due to local strain and defects due to the increased concentration of MWCNT. These defects can modify the crystal lattice, resulting in peak broadening and a slight shift in diffraction peaks. However, the refinement fit parameters R_p, R_{wp} and χ^2 show a minor increase with doping, but remain within widely accepted ranges for high-quality powder XRD refinements. As reported in previous literature studies, the acceptable χ^2 thresholds range from ~1 to 4 % for a good fit [40–42]. The χ^2 values for the present study vary between 2.5 and 2.95, which is in the acceptable range. The refined patterns do not show any extra peaks, indicating that the structure remains homogeneous with increased dopant concentration.

3.2. *Morphological analysis*

The FESEM micrographs of MWCNT, pristine ZnO and ZnO:xMWCNT NCs materials are shown in Fig. 5. Fig. 5(a and b) illustrated at different scales represent MWCNT as a nano-tube like structure. Fig. 5(c and d) at various scales revealed the pristine ZnO nanoparticles as agglomerated porous polygonal-shaped nanoparticles. The structure of pristine ZnO contains pores that indicate the release of gases such as NO_2 and CO_2 during synthesis. Fig. 5(e and f) depicts the FESEM images of ZnO:MWCNT NCs composed of 92 wt% ZnO and 8 wt% MWCNT. The images indicated that the interaction between ZnO nanoparticles and MWCNT occurred mainly on the surface but not within the deeper crystal structure of ZnO nanoparticles, which supports the absence of additional peaks as observed in the

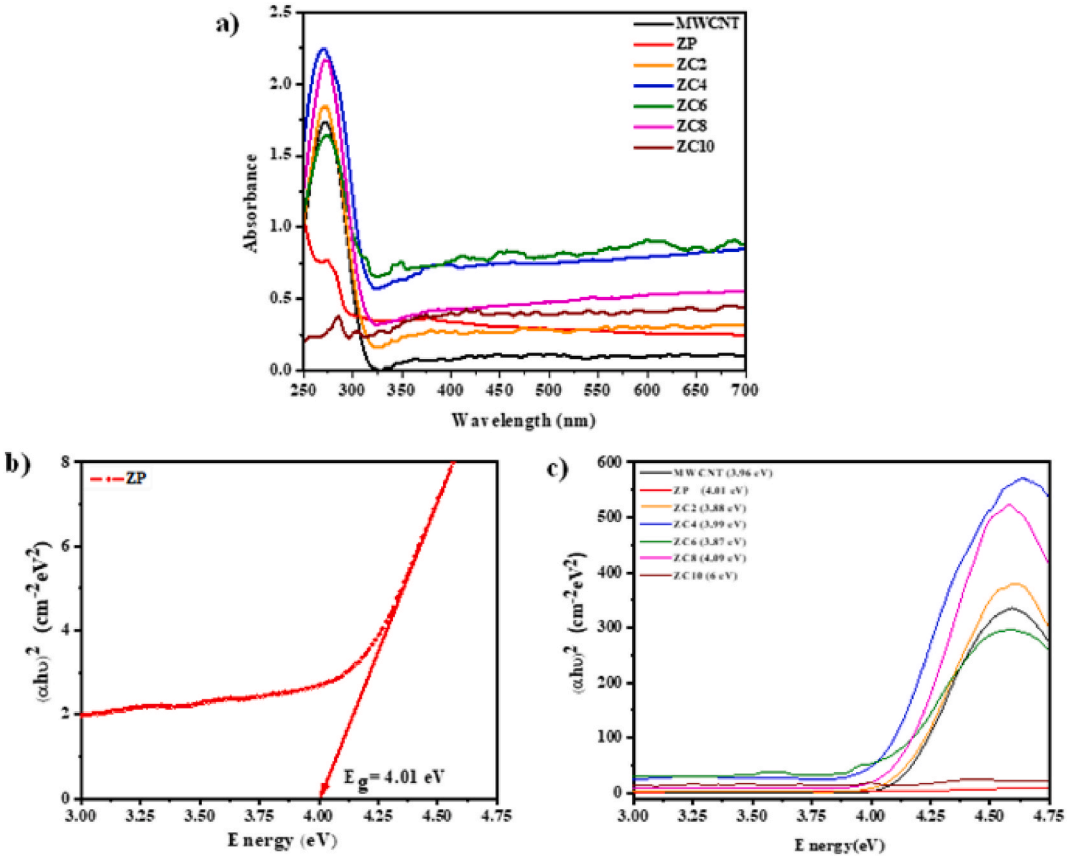

Fig. 9. a) UV–Vis absorbance spectra of MWCNT and ZnO:MWCNT **NCs**, b) Tauc plot of ZnO c) Tauc plot of MWCNTs and ZnO:MWCNT **NCs**.

Table 4
Photometric properties of MWCNT and ZnO:MWCNT nanocomposites.

Sample	CIE		CCT		CP	CCT (K)	E_g (eV)
	x	Y	u'	v'	%		
MWCNT	0.338	0.487	0.166	0.537	–	5377	3.96
ZP	0.156	0.023	0.211	0.07	97.63	1757	4.01
ZC2	0.157	0.022	0.213	0.068	97.76	1763	3.88
ZC4	0.156	0.023	0.211	0.071	97.63	1756	3.97
ZC8	0.156	0.024	0.21	0.071	97.37	1754	4.0
ZC10	0.157	0.022	0.212	0.071	97.76	1762	6.0

XRD analysis.

3.3. Elemental analysis

The energy dispersive X-ray analysis (EDAX) is a commonly used technique for identifying the composition of elements contained in the sample. The synthesis of ZnO: MWCNT NCs was confirmed through EDAX analysis. Fig. 6a reveals EDAX spectra peaks for Zn and O, authenticating that no other impurities were found in pristine ZnO. And Fig. 6b Shows the peak for Zn, C and O, indicating the uniform doping of MWCNTs within the Zn–O matrix. The inset table represents the percentage elemental compositions of the prepared samples. These results confirm the formation of both pure and doped NCs, supporting the results from XRD and FESEM for further investigations.

3.4. Infra-red spectroscopy analysis

The FTIR spectroscopy is one of the robust characterisation techniques for examining the functional groups and the arrangements of structural units in the synthesized samples. The FTIR spectra of the synthesized samples were obtained at room temperature within the

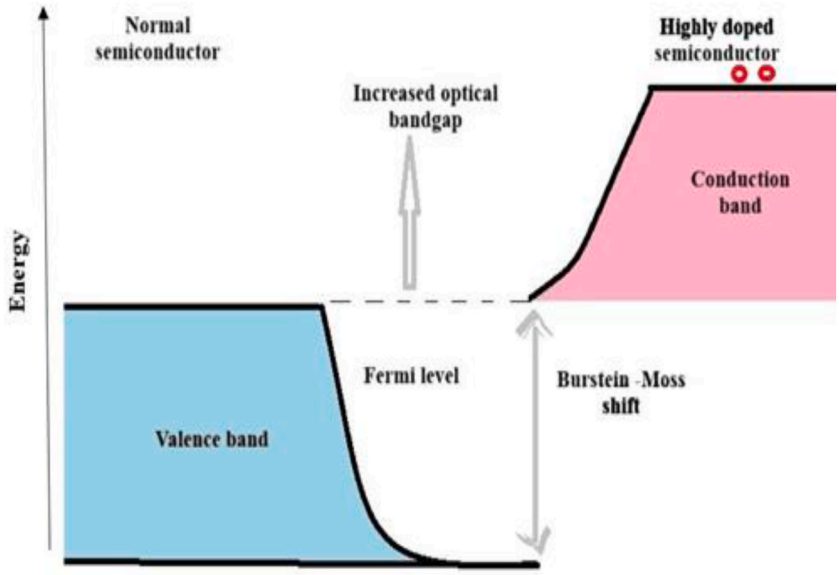

Fig. 10. Schematic diagram of B-M shift for bandgap tuning.

spectral range of 400–4000 $cm^{-1,}$ as illustrated in Fig. 7. The FTIR spectra are mainly divided into two regions, the fingerprint region and the functional group region. The fingerprint region below 1500 cm^{-1} is unique to the molecular structure of each compound. The region above 1500 cm^{-1} provides information about the functional groups present in the structure of organic compounds. Fig. 7a depicts the FTIR spectra of MWCNT. The peak at 1445 cm^{-1} is assigned as a unique characteristic of MWCNT [43,44]. Fig. 7b depicts the FTIR spectra of ZnO:MWCNT NCs. The peak positions in the range of 450–620 cm^{-1} correspond to the Zn–O stretching vibrations [45,46]. Further, the peaks observed in the range 1410–1640 cm^{-1} are attributed to the C–O and C═O symmetric stretching modes. This provides the evidence for the adsorption of MWCNTs with Zn–O. The broad absorption bands observed in the range of 3450–3580 cm^{-1} are assigned to the antisymmetric stretching vibrations of O–H hydroxyl groups [47].

3.5. Raman spectral analysis

Raman spectra of MWCNT, ZnO and NCs with 4 wt% and 8 wt% MWCNT were represented in Fig. 8. The D-band at 1346 cm^{-1} and G-band at 1576 cm^{-1} confirm the unique bands of MWCNTs and represent disordered defects and carbon layer in the MWCNTs [31]. The characteristic peaks of the synthesized ZnO are in agreement with standard wurtzite ZnO [45,48]. From Fig. 8, it can also be observed that the Raman spectra corresponding to the ZnO:MWCNT NCs exhibit the representative peaks of both ZnO and MWCNT [39]. The absence of any additional peaks in the Raman spectra is consistent with XRD, FESEM and FTIR results, confirming the formation of low-defect NCs.

3.6. UV–Vis absorption spectral analysis

The optical characteristics and energy bandgap of ZnO:MWCNT NCs are evaluated using UV–Vis spectroscopy across a wavelength range of 250–700 nm. To obtain the absorbance spectra, the MWCNT, the pristine ZnO and their NCs were ultrasonically dispersed in ethanol. The UV–Vis absorbance spectra of these findings are shown in Fig. 9a. The absorption bands for ZC4 and ZC8 samples were observed in the UV region (273 nm).

The Wood–Tauc's relation,

$$(\alpha h\nu)^n = k(h\nu - E_g) \tag{4}$$

is used to determine the bandgap energy. Here, 'α' stands for absorption coefficient and '$h\nu$' for photon energy at a specific wavelength, 'k' for energy-independent constant, 'E_g' for the material's energy bandgap and 'n' for transition type. For indirect and direct forbidden transitions, the value of n might be assigned as n = 1/3 or 2/3, respectively. For allowed direct or indirect transitions, n = 1/2 or 2. Since the synthesized NCs exhibit direct bandgap energy transitions, n = 2 is used in the above relation [51]. The numerical value of the bandgap corresponds to the intercept of the linearly fitted graph of $(\alpha h\nu)^2$ plotted on the y-axis against $h\nu$ on the x-axis as illustrated in Fig. 9b. The obtained values are listed in Table 4.

The noticeable differences in bandgap values confirm the formation of ZnO:MWCNT NCs. The bandgap tends to decrease as the concentration of MWCNT increases. This alliteration in the bandgap is a result of the quantum confinement effect. The optical characteristics of any NC material can be influenced when the particle dimensions approach the exciton radius, causing electrons and

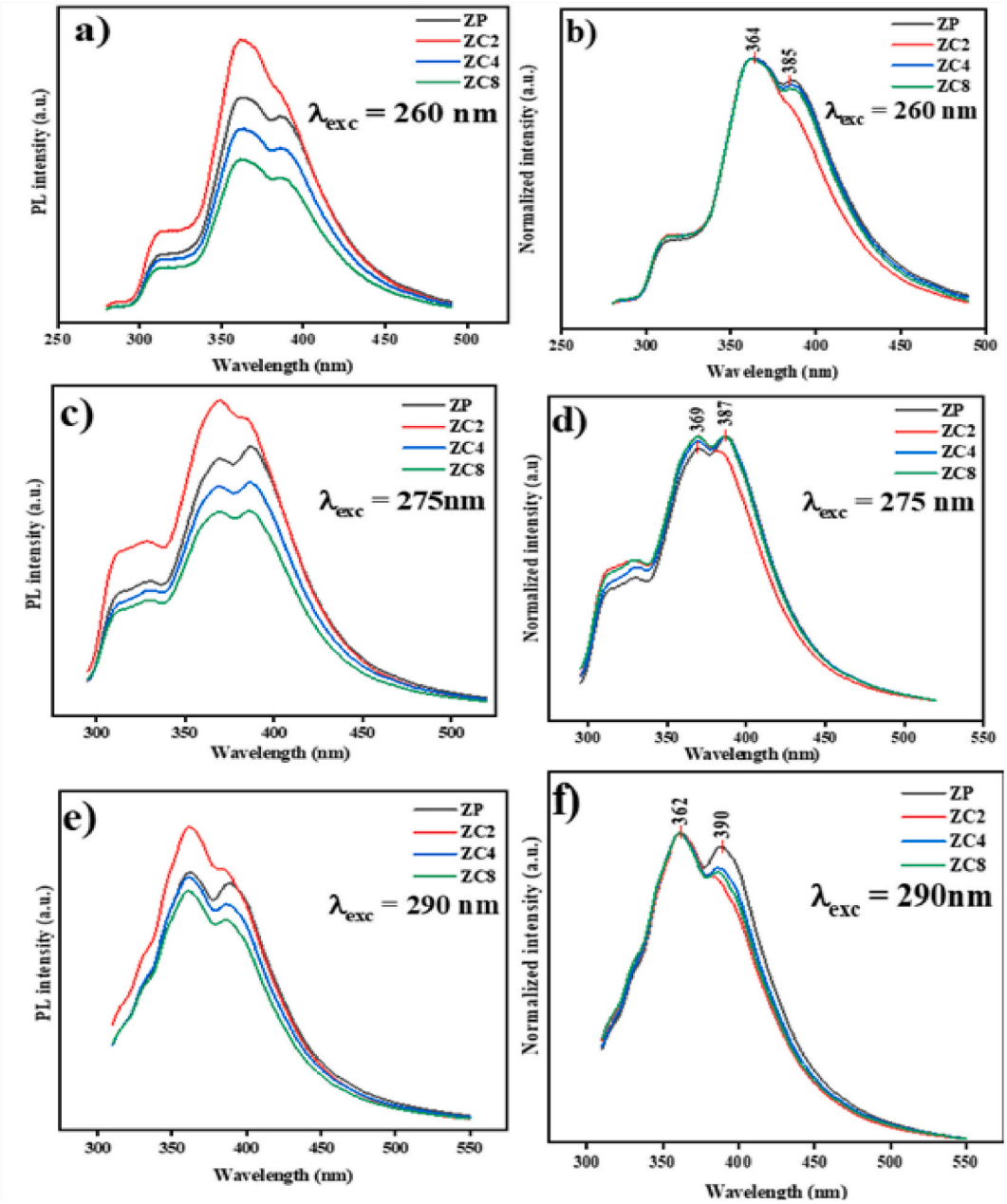

Fig. 11. (a), (c) and (e) PL emission spectra (b), (d) and (f) normalized emission spectra of ZnO and ZnO:MWCNT NCs excited at wavelengths 260,275 and 290 nm.

holes to be constrained to a narrow potential well [48–50]. Moreover, the observed variation in bandgap values can be elucidated by the Burstein–Moss (B–M) effect, where at elevated dopant concentrations the Fermi level migrates into the conduction band, resulting in absorption transitions arising between the valence band and the Fermi level in the conduction band, which is generally observed between the valence band and the bottom of the conduction band. The anomalously high bandgap value (6.0 eV) found in highly doped samples, such as ZC10, cannot be explained by surface defects alone. Although the B-M effect describes the increase in apparent bandgap with doping as it fills the conduction band states, pushing the Fermi level higher, this effect has certain restrictions.

At moderate MWCNT doping (ZC6 or ZC8), the bandgap tuning follows the B-M band filling effect. However, at very high doping (ZC10) at the interface leads to electron tunnelling and carrier saturation, pushing the semiconductor into a degenerate state [51–53]. As a result, the filled conduction band states cause a B-M shift, resulting in an increased bandgap value (6.0 eV) as represented schematically in the following Fig. 10.

Apart from this, the variation in band gap values may be attributed to increased surface defects due to doping, lattice strain,

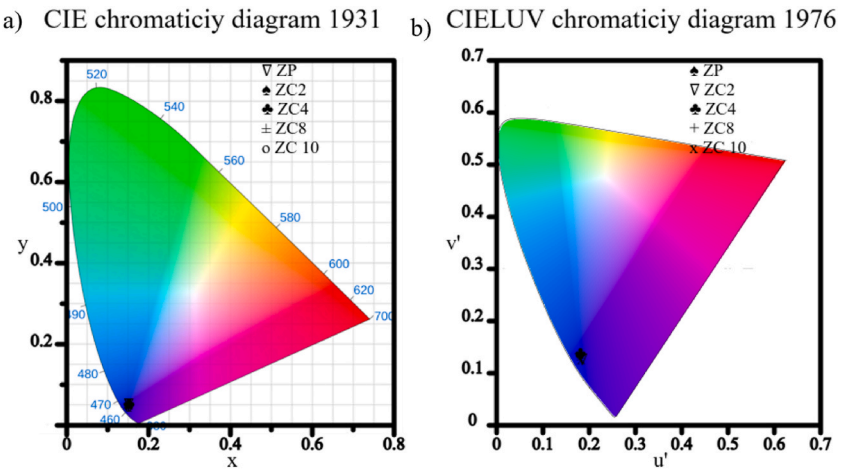

Fig. 12. a) CIE chromaticity diagram 1931 and b) CCT chromaticity diagram 1976 of ZnO and ZnO:MWCNT NCs.

Table 5
A comparative study of CIE and CCT values from the present study, compared to those of rare-earth-doped ZnO nanophosphors for LFP detection.

Sample	CIE coordinates	CCT (K)	Emission colour	LFP method	Substrates	LFP ridge details	Reference
ZAO:7mol%Eu^{3+}	(0.610,0.385)	1341	Orange-red	Powder dusting	Aluminium foil	Core, island, short ridge, hook, bifurcation, double bifurcation, bridge, scar, sweat pore	[62]
ZnO:La3+ (2mol%)	(0.226, 0.338)	6118	Blue-green	Powder dusting	Wood, mobile, bottle	Pocket whorl, crossing, plain arch	[63]
$InGaZnO_4$:2mol% Eu^{3+}	(0.614, 0.383)	–	Red	Powder dusting	Aluminium foil, bank note, weight paper, iron, glass	Right loop, delta, bifurcation, island, ending, short ridge, scars, sweat pores	[64]
$CaY_2Sb_2(ZnO_4)_3$:10 mol%Sm^{3+}	(0.585,0.414)	5674	Red	Powder dusting	Steel, plastic, glass, paper money	Ulnar loop, loop, spur, bifurcation, termination, bridge, sweat pore, crease	[65]
$ZnLa_4(SiO_4)_3O$: 20 mol%Eu^{3+}	(0.646, 0.354)	5233	Red	Powder dusting	Aluminium foil, glass, paper, plastic	Delta, right loop, bifurcation, ridge ending, sweat pores, crease	[66]
La_2CaZnO_5:1 mol% Er^{3+}	(0.316, 0.663)	5753	Green	Powder dusting	Paper, OHP, aluminium foil, plastic, steel, glass	Core, short ridge, ridge end, bifurcation, cross over, enclosure, eye, hook, delta, dot, independent ridge, scar, sweat pores	[67]
RGO/ZnO:1Eu^{3+}	–	–		Powder dusting	Leaf, aluminium foil, glass	Core, delta, loop, cross over, double bifurcation, incipient ridges, dot, hook, ridge end, bifurcation, encloser, sweat pores	[68]
ZnO:8 wt%MWCNT	(0.152, 0.084)	2223	Green	Powder dusting	Glass Sheet, acrylic sheet, granite, aluminium foil, wood	Whorl, bifurcation, island, lake, short ridge, trifurcation, bridge, loop, ridge ending, double bifurcation, delta, creases	**Present work**

crystallite size and shape and oxygen vacancies.

3.7. PL spectral analysis

PL spectroscopy is one of the most used analytical methods to study the emission properties of ZnO and ZnO:MWCNT NCs. The fundamental principle behind PL spectroscopy is that an electron gets excited from the valence band to the conduction band, followed by the energy being released as the electron returns to its ground state through radiative recombination. This electronic transition process provides important information on the purity of the sample, energy bandgap and defects associated with the sample.

The PL spectra of the synthesized ZnO and ZnO:MWCNT NCs were recorded at room temperature with an excitation wavelength of 260, 275 and 290 nm, as shown in Fig.(a), (c) and (e), respectively. The normalized emission spectra shown in Fig. 11(b)–(d) and (f) represent emission peaks at 364, 369 and 362 nm are purely attributed to the near-band-edge emission of ZnO. Additionally, peaks observed at 385, 387 and 390 nm correspond to shallow donor-acceptor pair recombination near the ZnO band edge. Since these emission peaks lie within the UV region of ZnO, no specific defect states were detected in the PL measurements [54–56].

The variation in PL intensity observed with the addition of MWCNT is primarily due to changes in near-band-edge recombination

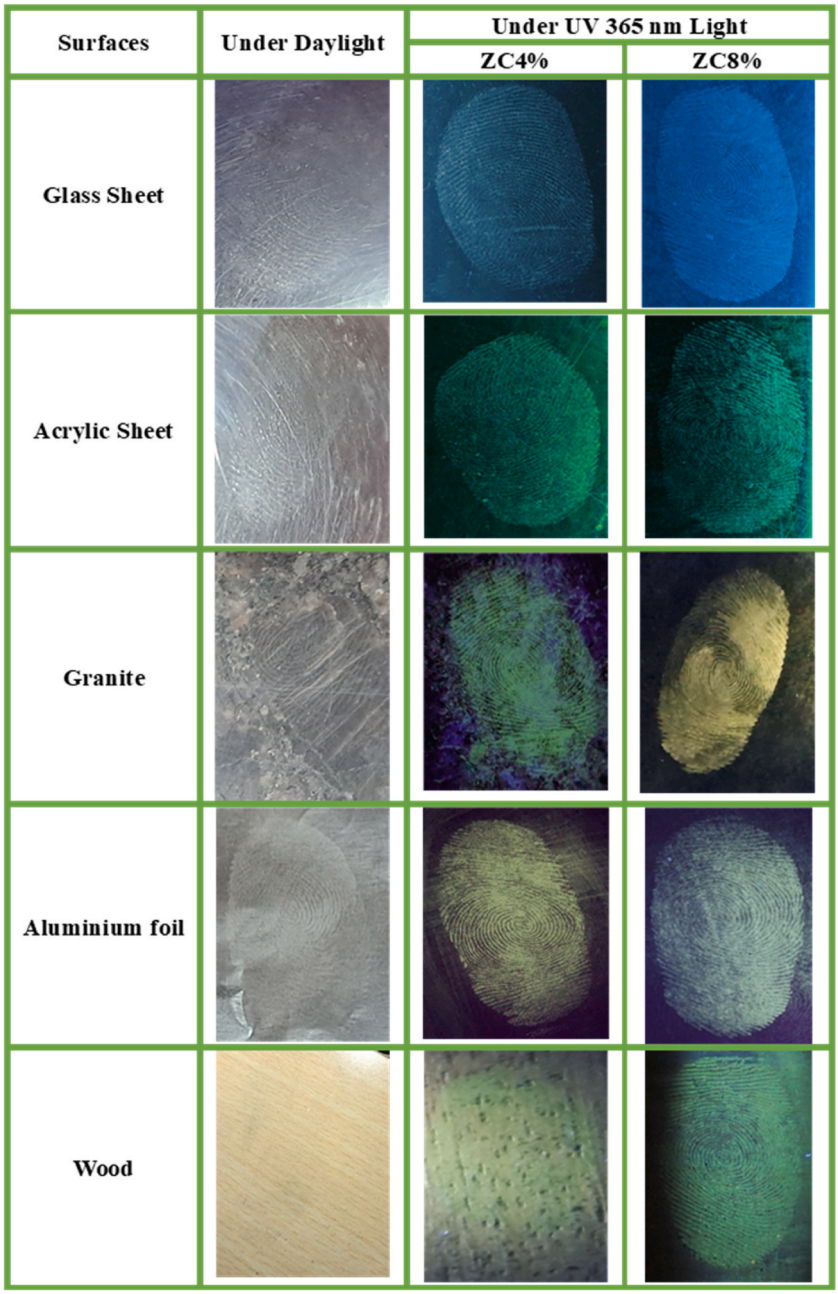

Fig. 13a. Digital images of **LFPs** captured on different non-porous and porous surfaces under daylight and UV-365 light.

dynamics and bandgap tuning. These PL results support the absence of additional peaks in XRD analysis. The absence of specific defect states in the PL spectra implies that the variation in the emission is due to band structure modification rather than defect states with an increase in MWCNT concentration. Moreover, the absence of excess defects in the sample was achieved by using the ex-situ ultrasonication method for synthesizing the nanocomposites. These low-defect NCs exhibited excellent stability against humidity, temperature and mechanical abrasion tests, making them a promising candidate for visualising latent fingerprints.

3.8. Photometric properties analysis

The effectiveness of a phosphor in producing colour can be assessed using colour coordinates and correlated colour temperature (CCT). The extent of a light source's coolness, neutrality, or warmth is determined by its CCT values. Commercial lighting typically uses cool colour sources with CCT levels exceeding 5000 K. In contrast, household appliances usually have CCT values below 5000K

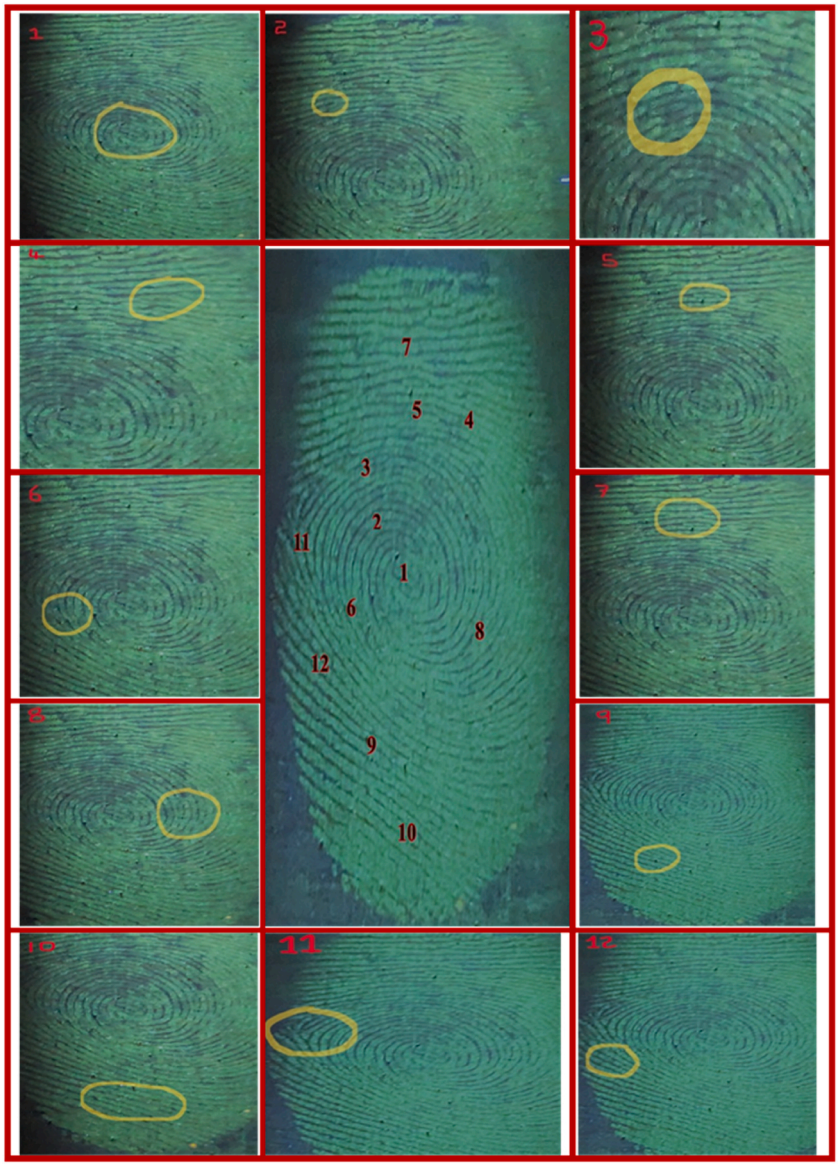

Fig. 13b. Detailed analysis of the developed **LFP** on the porous surface (wood) 1. Whorl, 2. Bifurcation, 3. Island, 4. Lake, 5. Short ridge, 6. Trifurcation, 7. Bridge, 8. Loop, 9. Ridge ending, 10. Double bifurcation, 11. Delta and 12. Creases.

and are typically termed as warm [55].

The CCT values of the samples were determined using McCamy's empirical formula as given by Ref. [57],

$$CCT = -437n^3 + 3601n^2 - 6861n + 5514.31 \tag{5}$$

In this formula, the difference (x-y) represents CIE coordinates, 'n' signifies the ratio of x-x_c to y-y_c, which denotes the inverse slope line; and x_c–y_c indicates chromaticity epicentres with the values $x_c = 0.332$ and $y_c = 0.186$. From the following equations [58], the u' and v' variables can be evaluated

$$u' = \frac{4x}{-2x + 12y + 3}, v' = \frac{9y}{-2x + 12y + 3} \tag{6}$$

The color purity of the prepared NCs was calculated using the following equation

$$Colorpurity = \frac{\sqrt{(xs - xi)^2 + (ys - yi)^2}}{\sqrt{(xd - xi)^2 + (yd - yi)^2}} \times 100\% \tag{7}$$

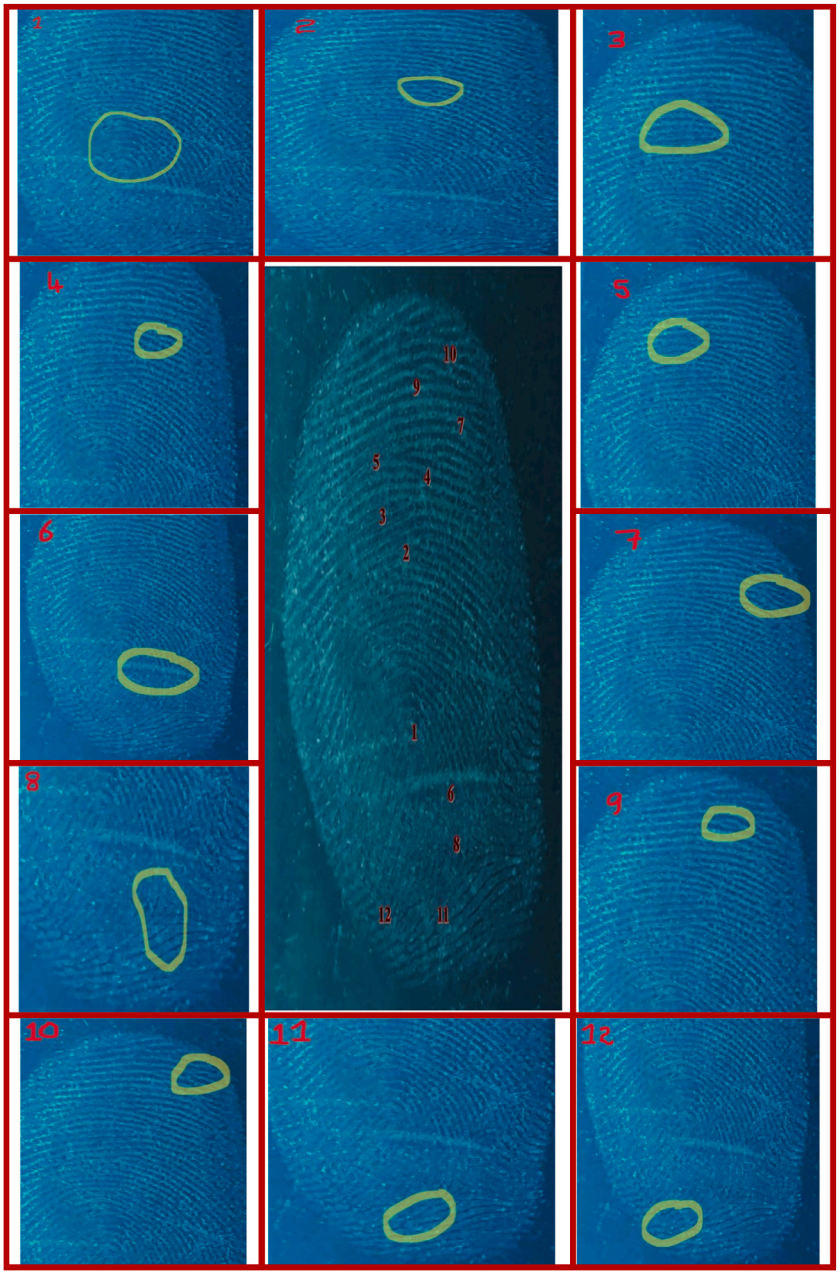

Fig. 13c. Detailed analysis of the developed LFP on the non-porous surface (glass sheet) 1. Arch, 2. Bifurcation, 3. Lake, 4. Bifurcation, 5. Bridge, 6. Scar, 7. Ridge ending, 8. Delta, 9. Eye, 10. Trifurcation, 11. Ridge ending and 12. Short ridge.

where (xi, yi) are the coordinates of the illuminant point, (xs:0.310, ys:0.316) are the source of light coordinates, and (xd:0.175, yd:0.005) are the dominant wavelength coordinates. The color purity of the prepared NCs is summarized in Table 4. The high color purity and low CCT values imply that these NCs might be suitable for warm white LED fabrication [59–61].

As per the CIE 1931 standard, Fig. 12a represents the CIE profile for the prepared composites. The acquired colour coordinates are found to be located within the cyan region. The CCT framework for the optimised phosphor is illustrated in Fig. 12b. A comparative table of CIE and CCT values from the present study, with the rare-earth-doped ZnO nanophosphors for LFP detection, is shown in Table 5. Overall, studies have shown that rare-earth-doped nanophosphors exhibit f-f transitions of dopant ions, display colour-specific, sharp, narrow emission bands, have lower contrast fingerprints, degrade upon thermal treatment, and are suitable for selective colour imaging only. On the other hand, the ZnO:MWCNT nanocomposites exhibit defect levels and interfacial charge transfer, high-intensity green emission, strong ridge visibility under UV exposure, and high thermal stability, making them suitable for multifunctional broad-band visualisation. Owing to the high cost and limited availability of rare-earth elements, MWCNT-doped

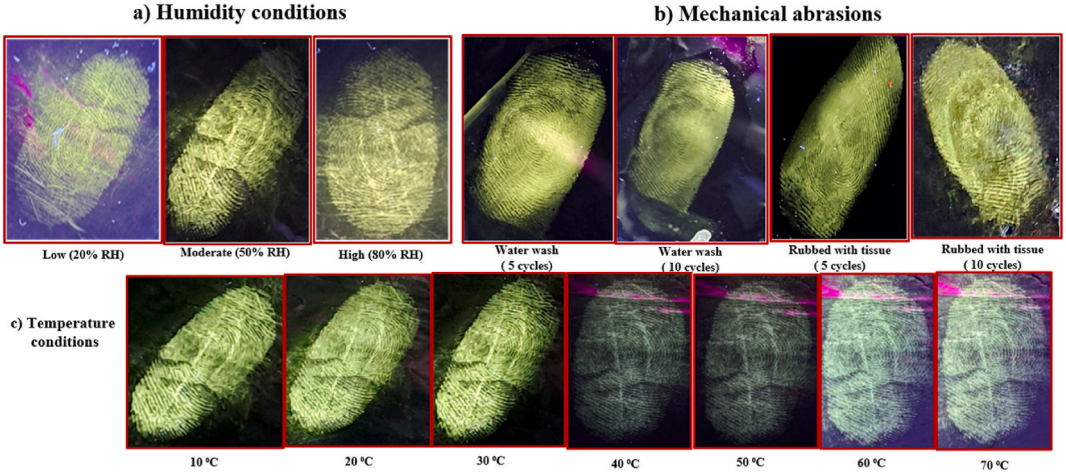

Fig. 14. Environmental stability tests conducted under various conditions.

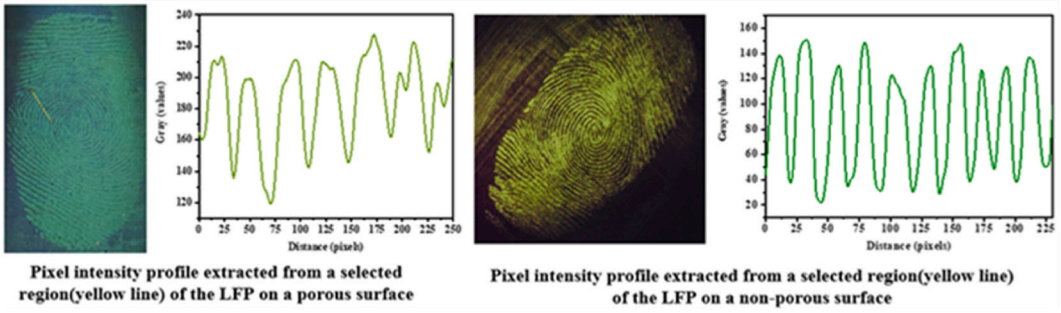

Fig. 15. Pixel intensity profile of the LFP.

nanocomposites offer a cost-effective and sustainable alternative for LFP detection.

3.9. Latent fingerprint (LFP) analysis

Human fingers have plenty of oil and sweat glands on their skin, which naturally produce fingerprints when they come into contact with objects. Sweat and sebum are continuously released during physical activity, which aids in transferring these materials to objects, causing FPs to form. Lipids, amino acids, chlorides and phosphates are among the complex mixture of organic and inorganic materials that make up these prints. To enhance the interaction between fingerprint residues and detection materials, phosphor powder is coated on the sebaceous secretions.

FPs were collected from the donors on different porous and non-porous surfaces like wood, aluminium foil, glass, acrylic sheet and granite. Based on the excellent properties of the synthesized ZnO:xMWCNT (x = 4,8 wt%) nanocomposites, they were effectively used for visualising LFPs. FPs were successfully detected on glass, aluminium foil, granite, acrylic and wood substrates using ZC4 and ZC8 nanocomposites as shown in Fig. 13a.

From the illustrations, all three levels of LFPs – the whorl, bifurcation, island, scar and ridge end are revealed. Fig. 13b. Displays a detailed analysis of the developed LFP on the porous surface (wood). Fig. 13c illustrates a detailed analysis of the developed LFP on the non-porous surface (glass sheet). Further, the stability of the prepared powders was assessed by ageing the LFPs up to 4 months, and they displayed comparable brightness. Based on the results obtained to investigate the detailed images of level I, level II and level III ridge characteristics in LFPs, it can be suggested that the synthesized nanocomposites can be efficiently used for investigating LFPs on various porous and non-porous surfaces.

The environmental stability tests were conducted under different humidity levels, mechanical abrasion conditions and temperatures and displayed the results in Fig. 14. Under humidity conditions and during mechanical abrasion tests (water wash), the presence of MWCNT in the nanocomposites shows a hydrophobic nature, preventing the water droplets from adhering to the fingerprints. This hydrophobic character of MWCNT enhances the durability of the nanocomposites. The thermal stability tests revealed that the visibility of the fingerprints increased with the temperature rise, showing that the nanocomposites are highly thermally stable.

The Fig. 15 shows the quantitative studies on ridge spacing that were conducted using ImageJ software. This study considered the pixel intensity profiles of fingerprints collected from both porous and non-porous surfaces. The average ridge spacing for fingerprints

collected from porous surfaces was found to be 21 pixels (~0.236 mm), and that for non-porous surfaces was found to be 22.3 pixels (~0.251 mm). The resolution ratio for a fingerprint on a porous surface was found to be 4.24 ridges/mm, and that of a non-porous surface is 3.984 ridges/mm. These results align with the present literature [69]. The high-density fingerprints reveal the donor as a female [70].

4. Conclusion

The ZnO:MWCNT NCs synthesized via low-temperature solution combustion and ultrasonication were used to visualise LFPs. The reduced size of the nanocomposites revealed the ridge characteristics up to levels I, II and III. The details of the developed LFPs subjected to environmental stability tests, including varying humidity, temperature, and mechanical abrasion, were discussed in detail. The average ridge spacing of 0.236 mm and 0.251 mm, and a resolution ratio of 4.24 and 3.984 ridges/mm, revealed the gender of the donor. The CIE, CCT, and colour purity values of NCs make them a promising candidate for the fabrication of warm LEDs. Overall, studies indicate that MWCNT doping can be a suitable alternative for rare earth elements to enhance the luminescent properties of nanocomposites.

CRediT authorship contribution statement

Basavajyothi Khapate: Writing – review & editing, Writing – original draft, Software, Resources, Methodology, Investigation, Formal analysis, Data curation, Conceptualization. **Bhavani Betadur:** Investigation, Data curation. **Madhura N. Talwar:** Writing – review & editing, Software, Formal analysis. **Asha P. Shirni:** Data curation. **Milana Nagaraj:** Data curation. **Kotresh M. Goudar:** Writing – review & editing, Visualization, Validation, Software, Resources, Methodology, Conceptualization. **Gnanaprakash A.P.:** Writing – review & editing, Validation, Resources. **Pushpa N.:** Visualization, Validation, Supervision.

Declaration of competing interest

The authors declare that they have no conflict of interest.

Appendix A. Supplementary data

Supplementary data to this article can be found online at https://doi.org/10.1016/j.micrna.2025.208513.

Data availability

Data will be made available on request.

References

[1] S. Bansal, S.S. Nayak, I. Dave, The role of forensic science and digital technology in enhancing investigation efficacy: an analytical study, Cuestiones De Fisioterapia 53 (3) (2024) 2332–2359.
[2] M. Di Nunzio, J. De Alcaraz-Fossoul, V. Maroto-Nouveau, C. Camprubí-Aumatell, C. Barrot-Feixat, From dactyloscopy to the minimum surface requirement (MSR): a metric to assess and obtain suitable human STR profiles, Forensic Sci. Int. 368 (2025) 112408.
[3] R.K. Jain, S.N. Ananya, P.J. Anand, D. Sunil, A comprehensive review on the use of rare earth-based luminophores for latent fingerprint detection, Microchem. J. (2025) 112749.
[4] G.S. Bumbrah, M. Jani, D.S. Bhagat, K. Dalal, A. Kaushal, K. Sadhana, G. Sriramulu, A. Das, Zinc oxide nanoparticles for detection of latent fingermarks on nonporous surfaces, Mater. Chem. Phys. 278 (2022) 125660.
[5] R. Dhaneshwar, M. Kaur, M. Kaur, An investigation of latent fingerprinting techniques, Egypt. J. Food Sci. 11 (1) (2021) 33.
[6] I.S. Pruthviraj, B.R. Krushna, S.C. Sharma, K. Manjunatha, S.Y. Wu, H.H. Chiu, Lo Wei-Che, Mohapatra Liza, K.P. Aravind, Burnice Nalina Kumari, H. Nagabhushana, Exploring Mg2+ doped CoCr2O4 nanoparticles: eco-friendly pigments, radiation dosimeters and latent fingerprint visualization, Mater. Sci. Eng., B 317 (2025) 118217.
[7] R. Kaur, N. Kaur, P. Singh, Rescuing fluorescence with steric hindrance: perylene diimide based powder for latent fingerprint imaging, Forensic Chemistry 44 (2025) 100662.
[8] M. Wang, M. Li, A. Yu, Y. Zhu, M. Yang, C. Mao, Fluorescent nanomaterials for the development of latent fingerprints in forensic sciences, Adv. Funct. Mater. 27 (14) (2017) 1606243.
[9] International Fingerprint Research Group Collaboration, Guidelines for the assessment of fingermark detection techniques, J. Forensic Ident. 64 (2) (2014) 174–200.
[10] E. Prabakaran, K. Pillay, Nanomaterials for latent fingerprint detection: a review, J. Mater. Res. Technol. 12 (2021) 1856–1885.
[11] H.R. Girisha, D.R. Lavanya, P.B. Daruka, S.C. Sharma, H. Nagabhushana, Anti-counterfeiting, latent fingerprint detection and optical thermometry using a multi-stimulus down-converting La2CaZnO5: Er3+ phosphor, Opt. Mater. 134 (2022) 113053.
[12] D. He, L. Guan, H. Sun, F. Zeng, F. Li, L. Zhang, W. Li, H. Deng, D. Zhang, R. Yu, CaY2Sb2 (ZnO4) 3: Sm3+ phosphors with high thermal stability for high CRI w-LEDs and visualization of latent fingerprints, Ceram. Int. (2025).
[13] M. Dhanalakshmi, H. Nagabhushana, G.P. Darshan, R.B. Basavaraj, B.D. Prasad, Sonochemically assisted hollow/solid BaTiO3: Dy3+ microspheres and their applications in effective detection of latent fingerprints and lip prints, J. Sci. Adv. Mater. Devices 2 (1) (2017) 22–33.
[14] S. Paikray, S.K. Ray, P. Nayak, A.K. Sahoo, S.N. Prusty, S. Dash, S.S. Nanda, Comparative analysis of Sm3+-doped BaWO4 and CaWO4 phosphors: properties and application in latent fingerprints and anti-counterfeiting, J. Alloys Compd. 1010 (2025) 177666.

[15] K.V. Babu, C.G. Renuka, H. Nagabhushana, Mixed fuel approach for the fabrication of TiO2: Ce3+ (1–9 mol%) nanophosphors: applications towards wLED and latent finger print detection, Ceram. Int. 44 (7) (2018) 7618–7628.
[16] K.N. Narasimhamurthy, G.P. Darshan, S.C. Sharma, H.B. Premkumar, H. Adarsha, H. Nagabhushana, Surface functionalized inorganic phosphor by grafting organic antenna for long term preservation of latent fingerprints and data-security applications, J. Colloid Interface Sci. 600 (2021) 887–897.
[17] G. Lu, Y. Zhang, J. Song, Y. Jing, X. Li, R. Qin, B.D. Zhai, J. Jiang, Y. Wang, H. Wang, Enhanced red upconversion luminescence in Fe3+-activated NaYF4: yb, Er nanocrystals for rapid latent fingerprint recognition, J. Lumin. 282 (2025) 121218.
[18] K.C. Sushma, S. Kumar, G. Nagaraju, D.P. Aarti, M.M. Reddy, M.S. Rudresha, R.B. Basavaraj, Color tunable SrZrO3: Sm3+ nanopowders with satisfactory photoluminescent, band engineering properties for warm white LEDs and advanced forensic applications, J. Mol. Struct. 1254 (2022) 132302.
[19] E.I. Naik, H.B. Naik, B.K. Swamy, R. Viswanath, I.S. Gowda, M.C. Prabhakara, K. Chetankumar, Influence of Cu doping on ZnO nanoparticles for improved structural, optical, electrochemical properties and their applications in efficient detection of latent fingerprints, Chem. Data Collect. 33 (2021) 100671.
[20] B. Flores, M. Guzman, R. Grieseler, A. Quiroz, L. Malet, S. Godet, Synthesis of zinc oxide nanoparticles and their potential application in the detection of latent fingerprints, J. Cluster Sci. 36 (2) (2025) 1–24.
[21] G. Lu, R. Qin, D. Zhai, T. Wan, J. Jiang, D. Zhang, P. Zhang, Y. Wang, H. Wang, Mn2+-activated NaYF4: yb, Er red-emitting nanophosphors for accurate latent fingerprint identification by an Artificial intelligence program, J. Alloys Compd. 1002 (2024) 175269.
[22] Pradhan, P. P., Rakshita, M., Sharma, A. A., Durga Prasad, K. A. K., and Kumar, R. R. Investigation of Eu3+-Doped Y2srzno5 Nanophosphor as a Novel Fluorescent Marker for Easy Detection of Latent Fingerprints at the Crime Scene.
[23] B.R. Krushna, H.H. Chiu, M.K. Ho, T.E. Hsu, B.L. Lyu, W.C. Lo, B. Subramanian, K. Manjunatha, H. Nagabhushana, Investigating Fe-doped yttrium oxide nanophosphors for enhanced latent fingerprint visualization and deep learning analysis, Mater. Today Sustain. 25 (2024) 100629.
[24] X. Ouyang, R. Liu, X. Hu, J. Li, R. Tang, X. Jin, S. Chen, X. Yao, B. Deng, H. Geng, R. Yu, Preparation, characterization, and application of a red phosphor Ca2InTaO6: Eu3+ in w-LEDs and latent fingerprint detection, J. Alloys Compd. 939 (2023) 168715.
[25] S. Dwivedi, R. Sharma, Y. Sharma, Electroconductive properties in doped spinel oxides, Opt. Mater. 37 (2014) 656–665.
[26] V. Kumar, O.M. Ntwaeaborwa, T. Soga, V. Dutta, H.C. Swart, Rare earth doped zinc oxide nanophosphor powder: a future material for solid state lighting and solar cells, ACS Photonics 4 (11) (2017) 2613–2637.
[27] D. Daksh, Y.K. Agrawal, Rare earth-doped zinc oxide nanostructures: a review, Reviews in nanoscience and nanotechnology 5 (1) (2016) 1–27.
[28] G. Pawar, R.C. Ewing, Recent advances in the global rare-earth supply chain, MRS Bull. 47 (3) (2022) 244–249.
[29] D. Eder, Carbon nanotube– inorganic hybrids, Chem. Rev. 110 (3) (2010) 1348–1385.
[30] Z.T. Banizi, M. Seifi, M.B. Askari, S.B. Dehaghi, Photoluminescence and photocatalytic studies of cadmium sulfide/multiwall carbon nanotube (CdS/MWCNT) nanocomposites, Optik 158 (2018) 882–892.
[31] M.N. Talwar, A. Gangadhar, M. Manoharan, R. Manimozhi, S. Srikantaswamy, R.R. Kumar, A.G. Prakash, Humidity enhanced ammonia gas sensing by Ga2O3/MWCNT nanocomposite at room temperature, Mater. Sci. Semicond. Process. 175 (2024) 108255.
[32] B.K. Grandhe, V.R. Bandi, K. Jang, S. Ramaprabhu, H.S. Lee, D.S. Shin, S.S. Yi, J.H. Jeong, Multi wall carbon nanotubes assisted synthesis of YVO4: Eu3+ nanocomposites for display device applications, Compos. B Eng. 43 (3) (2012) 1192–1195.
[33] M. Krajewski, P.H. Lee, S.H. Wu, K. Brzozka, A. Malolepszy, L. Stobinski, M. Tokarczyk, G. Kowalski, D. Wasik, Nanocomposite composed of multiwall carbon nanotubes covered by hematite nanoparticles as anode material for Li-ion batteries, Electrochim. Acta 228 (2017) 82–90.
[34] M. Doğan, Z. Bicil, B.K. Kizilduman, Y. Turhan, F. an Pehlivan, Functionalization and metal doping of MWCNTs for hydrogen storage, J. Energy Storage 122 (2025) 116653.
[35] Z. Zhao, C. Xie, Y. Liu, Z. Zhao, Y. Ouyang, Y. Song, T. Shi, Early-age thermal cracking performance of carbon nanotube modified face slab concrete, Constr. Build. Mater. 433 (2024) 136666.
[36] M. Ahmadipour, M. Arjmand, A.T. Le, S.L. Chiam, Z.A. Ahmad, S.Y. Pung, Effects of multiwall carbon nanotubes on dielectric and mechanical properties of CaCu3Ti4O12 composite, Ceram. Int. 46 (12) (2020) 20313–20319.
[37] H.K. Jazi, M. Sarafbidabad, M.B. Henda, M. Ahmadipour, The effect of laser surface texturing on ZnO/MWCNT nanocomposite modified screen-printed carbon electrode for non-enzymatic glucose biosensor, Diam. Relat. Mater. 151 (2025) 111845.
[38] M.R. Ardani, A.L. Pang, U. Pal, R. Zheng, A. Arsad, A.A. Hamzah, M. Ahmadipour, Ultrasonic-assisted polyaniline-multiwall carbon nanotube photocatalyst for efficient photodegradation of organic pollutants, J. Water Proc. Eng. 46 (2022) 102557.
[39] R.A. Zargar, M. Arora, Alshahrani, M. Shkir, Screen printed novel ZnO/MWCNTs nanocomposite thick films, Ceram. Int. 47 (5) (2021) 6084–6093.
[40] A. Adam, Rietveld refinement of the semiconducting system Bi2− xFexTe3 from X-ray powder diffraction, Mater. Res. Bull. 42 (12) (2007) 1986–1994.
[41] A.S. Sathishkumar, K. Arun Balasubramanian, T. Ramkumar, Structural characterization of ZnO, CuO and Fe2O3 nanoparticles: evaluation of rietveld refinement, Tierarztl. Prax. 40 (2020) 1139–1154.
[42] J.E. Morales-Mendoza, F. Paraguay-Delgado, J.D. Moller, G. Herrera-Pérez, N. Pariona, Structure and optical properties of ZnO and ZnO2 nanoparticles, J. Nano Res. 56 (2019) 49–62.
[43] H.S. Vaziri, A. Shokuhfar, S.S.S. Afghahi, Synthesis of WS2/CNT hybrid nanoparticles for fabrication of hybrid aluminum matrix nanocomposite, Mater. Res. Express 7 (2) (2020) 025034.
[44] J.H. Lehman, M. Terrones, E. Mansfield, K.E. Hurst, V. Meunier, Evaluating the characteristics of multiwall carbon nanotubes, Carbon 49 (8) (2011) 2581–2602.
[45] A. Sharma, B.P. Singh, S. Dhar, A. Gondorf, M. Spasova, Effect of surface groups on the luminescence property of ZnO nanoparticles synthesized by sol–gel route, Surf. Sci. 606 (3–4) (2012) L13–L17.
[46] S. Fakhari, M. Jamzad, H. Kabiri Fard, Green synthesis of zinc oxide nanoparticles: a comparison, Green Chem. Lett. Rev. 12 (1) (2019) 19–24.
[47] M. Zargham, M.F. Khan, R.A. Rehman, A. Rakha, R. Nazir, M. Salman, A. Munawar, Role of doped ZnO variants for the development of latent fingerprint, Inorg. Chem. Commun. 162 (2024) 112269.
[48] C. Kalyani, I.S. Reddy, P. Raju, P.M.S. Raju, Study of structural, optical properties and band structure analysis of zinc oxide substituted with manganese, Ceram. Int. (2025).
[49] P. Kaur, A. Kaur, S. Singh, S. Thakur, L. Singh, Comprehensive analysis of crystal structure, optical and luminescent behavior of Fe doped MgO nanophosphors, Optik 219 (2020) 164742.
[50] K.R. Bhagya, R.B. Basavaraj, K.R. Jyothi, H. Nagabhushana, M.V. Murugendrappa, A.G. Prakash, N.M. Nagabhushan, V.N. Hegde, Dy3+ doped Y2MoO6 nanopowders for white light emission: spectroscopic and transport properties for optoelectronic and energy harvesting applications, Colloid and Interface Science Communications 43 (2021) 100447.
[51] A. Kadari, K. Mahi, R. Mostefa, M. Badaoui, A. Mameche, D. Kadri, Optical and structural properties of Mn doped CaSO4 powders synthesized by sol-gel process, J. Alloys Compd. 688 (2016) 32–36.
[52] P. Kaur, A. Kaur, S. Singh, L. Singh, MgO: li+ phosphor: in depth analysis of its structural, optical and thermoluminescent behavior after gamma irradiation, Opt. Mater. 120 (2021) 111435.
[53] Y. Shen, X. Yang, Y. Bian, K. Nie, S. Liu, K. Tang, R. Zhang, S. Gu, First-principles insights on the electronic and optical properties of ZnO@ CNT core@ shell nanostructure, Sci. Rep. 8 (1) (2018) 15464.
[54] P. Parida, J. Patra, V.R. Singh, S.K. Reddy, V.K. Verma, Structural, thermal, and optical characterization of ZrC-ZnO composites for UV/Blue light emission, Opt. Mater. (2025) 117502.
[55] J. Rosowska, J. Kaszewski, M. Krajewski, A. Małolepszy, B.S. Witkowski, Ł. Wachnicki, L.-I. Bulyk, P. Sybilski, M. Godlewski, M.M. Godlewski, Growth of ZnO nanoparticles using microwave hydrothermal method—search for defect-free particles, Nanomaterials 15 (3) (2025) 230.
[56] S.S. Kurbanov, H.C. Jeon, Z.S. Shaymardanov, R.Y. Rakhimov, T.W. Kang, Photoluminescence from porous textured ZnO films grown by chemical bath deposition, J. Lumin. 170 (2016) 168–173.
[57] M.R. Ardani, A.L. Pang, U. Pal, M.A.S.M. Haniff, A.G. Ismail, A.A. Hamzah, W.A. Khanday, M. Ahmadipour, Ultrasonic-assisted of TiO2-MWCNT nanocomposite with advanced photocatalytic efficiency for elimination of dye pollution, Diam. Relat. Mater. 137 (2023) 110066.

[58] H.R. Girisha, B.D. Prasad, B.R. Krushna, H.M. Sujatha, S. Devaraja, S.C. Sharma, C. Sridhar, D. Francis, K. Manjunatha, S.Y. Wu, G.V. Kumar, H. Nagabhushana, Versatile properties of BaGd2ZnO5: Ho3+ nanomaterial: compatible towards solid state lightning, anti-counterfeiting and biomedical applications, Inorg. Chem. Commun. 159 (2024) 111711.
[59] N.H. Deepthi, R.B. Basavaraj, S.C. Sharma, J. Revathi, S. Sreenivasa, H. Nagabhushana, Rapid visualization of fingerprints on various surfaces using ZnO superstructures prepared via simple combustion route, J. Sci. Adv. Mater. Devices 3 (1) (2018) 18–28.
[60] S. Limbu, L.R. Singh, A comparative study of a tunable body-centered cubic (I) red-emitting nanophosphor for warm WLED applications, J. Solid State Chem. 308 (2022) 122929.
[61] S. Wang, Q. Sun, B. Devakumar, J. Liang, L. Sun, X. Huang, Novel high color-purity Eu3+-activated Ba3Lu4O9 red-emitting phosphors with high quantum efficiency and good thermal stability for warm white LEDs, J. Lumin. 209 (2019) 156–162.
[62] M. Gagana, B.R. Krushna, S.C. Sharma, K.J. Salwe, A. George, M.R. Sanjana, B. Kar, K.V. Archana, S. Pasha, K. Manjunatha, S.Y. Wu, H. Nagabhushana, Luminescent carbon dots encapsulating in Eu3+ doped gahnite spinel nanocomposite for boosting thermal sensing, advanced level III detection and intelligent anti-counterfeiting applications, Mater. Today Sustain. 27 (2024) 100872.
[63] H.N. Shivananjaiah, K.S. Kumari, M.S. Geetha, Green mediated synthesis of lanthanum doped zinc oxide: study of its structural, optical and latent fingerprint application, J. Rare Earths 38 (12) (2020) 1281–1287.
[64] J. Lian, X. Miao, Y. Ran, R. Liu, X. Liu, L.L. Zheng, R. Yu, Synthesis, characterization and application of an orange-red-emitting InGaZnO4: Eu3+ phosphor in latent fingerprint and security ink, Solid State Sci. 157 (2024) 107702.
[65] D. He, L. Guan, H. Sun, F. Zeng, F. Li, L. Zhang, W. Li, H. Deng, D. Zhang, R. Yu, CaY2Sb2 (ZnO4) 3: Sm3+ phosphors with high thermal stability for high CRI w-LEDs and visualization of latent fingerprints, Ceram. Int. (2025).
[66] J. Kong, H. Su, C. Li, S. Cheng, Y. Wang, Y. Ran, Y. Li, Y. Shang, S. Xie, R. Yu, Synthesis and luminescence properties of oxyapatite-type ZnLa4 (SiO4) 3O: Eu3+ phosphor for high CRI w-LEDs, latent fingerprints, and security ink, Ceram. Int. 49 (23) (2023) 39329–39341.
[67] H.R. Girisha, D.R. Lavanya, P.B. Daruka, S.C. Sharma, H. Nagabhushana, Anti-counterfeiting, latent fingerprint detection and optical thermometry using a multi-stimulus down-converting La2CaZnO5: Er3+ phosphor, Opt. Mater. 134 (2022) 113053.
[68] P.S. Kumar, N.R. Nadar, S.C. Sharma, B.K. Das, Development of solution combustion-synthesized RGO/ZnO: 1Eu3+ nanocomposite for supercapacitor and fingerprint visualization applications, Diam. Relat. Mater. 153 (2025) 112103.
[69] S.C. Chua, E.K. Wong, A.W.C. Tan, Fingerprint ridge distance estimation: a mathematical modeling, Int. J. Comput. Appl. 126 (15) (2015).
[70] S. Sharma, R. Shrestha, K. Krishan, T. Kanchan, Sex estimation from fingerprint ridge density. A review of literature, Acta Biomed.: Atenei Parmensis 92 (5) (2021) e2021366.